



# Heliospheric Maps from Cassini INCA Early in the Cruise to Saturn

J. H. Westlake<sup>1</sup>, D. G. Mitchell<sup>1</sup>, M. Gkioulidou<sup>1</sup>, K. Dialynas<sup>2</sup>, I. J. Cohen<sup>1</sup>, S. Krimigis<sup>1</sup>, R. B. Decker<sup>1</sup>,  
D. L. Turner<sup>1</sup>, A. K. Higginson<sup>1</sup>, G. Clark<sup>1</sup>, and C. P. Paranicas<sup>1</sup>

<sup>1</sup>Johns Hopkins University Applied Physics Laboratory, Laurel, MD 20723, USA

<sup>2</sup>Office of Space Research and Technology, Academy of Athens, Athens 10679, Greece

Received 2020 May 18; revised 2020 September 29; accepted 2020 September 30; published 2020 October 21

## Abstract

We present new energetic neutral atom (ENA) maps from the Ion and Neutral Camera (INCA) instrument on Cassini from the year 2000, prior to Cassini's encounter with Jupiter. These maps are the first produced for the year 2000 and are the only maps with comprehensive spatial coverage from the peak of solar cycle 23. These ENA maps span the energy range from 5.2 to 55 keV covering the pickup to suprathermal energy range. These maps represent a novel glimpse into the influence of the solar cycle on the structure of the outer heliosphere, specifically on the heliosheath where pickup and suprathermal ions dominate. The observations are consistent with the picture of the heliosheath from previous observations by the Cassini, Interstellar Boundary Explorer (IBEX), and Voyager missions. These maps have some consistent spatial features to maps produced by Cassini during solar cycle 24 such as reduced intensities in the mid-latitude basins. These maps also have distinct spatial features such as enhanced intensities at the poles and reduced intensities at the low-latitude flanks. These maps do not indicate a strong intensity increase in the regions adjacent to the nose and also show an intensity increase in the regions adjacent to the tailward direction.

*Unified Astronomy Thesaurus concepts:* [Heliosphere \(711\)](#); [Heliosheath \(710\)](#); [Solar wind \(1534\)](#)

## 1. Introduction

Energetic neutral atoms (ENAs) are generated at the boundaries of the heliosphere (Gruntman et al. 2001) where the outflowing solar wind and pickup ions (PUIs) charge exchange with incoming cold neutral atoms from the local interstellar medium (LISM). The interaction of the solar wind with the LISM has two important boundaries: the heliopause, where the solar wind pressure can no longer stand off the interstellar medium, and the termination shock, where the solar wind has sufficiently slowed below the fast magnetosonic speed (e.g., Richardson 2010). The region between the termination shock and the heliopause is the heliosheath, which contains a population of suprathermal particles that play a significant role in the pressure balance. The confluence of the hot plasma and suprathermal pressure in the inner heliosheath balance the external pressures upon the heliosphere defining the shape and the size of the interaction between the solar system and interplanetary space.

The ENA maps produced by the Interstellar Boundary Explorer (IBEX) mission (McComas et al. 2009a) and the Cassini/Ion and Neutral Camera (INCA) instrument (Krimigis et al. 2009) reveal the interactions of the solar wind, suprathermal particles, and the LISM. ENA measurements from IBEX and INCA along with the in situ measurements from Voyagers 1 and 2 (Decker et al. 2005; Burlaga et al. 2013, 2019; Gurnett et al. 2013; Krimigis et al. 2013, 2019; Stone et al. 2013, 2008, 2019; Gurnett & Kurth 2019; Richardson et al. 2019) produce our current understanding of this region of space. The IBEX-Hi measurements (Funsten et al. 2009) span from 0.52 to 6.0 keV FWHM (McComas et al. 2014a) covering the solar wind to PUI energy ranges and show a complex interaction composed of a globally distributed flux (Funsten et al. 2009; McComas et al. 2009b; Schwadron et al. 2011) and

an intense ribbon of enhanced ENA emissions (Funsten et al. 2009; Fuselier et al. 2009; McComas et al. 2009b; Schwadron et al. 2009) that forms a circle toward the heliospheric nose, between the V1 and V2 directions, in ecliptic coordinates and is thought to be generated from a secondary ENA charge exchange process (McComas et al. 2009b, 2014b; Heerikhuisen et al. 2009). The higher-energy Cassini/INCA ENA maps span 5.2 to 55 keV and appear dominated by the suprathermal particles that primarily populate the heliosheath between the termination shock and the heliopause (Krimigis et al. 2009; Dialynas et al. 2013, 2017a, 2019). Using the full array of measurements available between IBEX, INCA, and the Voyagers gives a more complete picture of the particle populations that reside in the outer heliosphere.

The majority of the Cassini/INCA data from 2003 to 2014 were analyzed by Dialynas et al. (2017a), showing significant solar cycle dependence in both the intensity of ENAs observed and the structure of the maps. The combined Cassini/INCA maps and the Voyager/Low-Energy Charged Particle (LECP) instrument in situ measurements in overlapping energy bands present a compelling case that the >30 keV ions distribute themselves throughout the heliosheath by a mechanism faster than pure advection with the thermal solar wind ions. The variations in the measured ENA intensities are related to the decline and rise of the solar cycle, as manifested in the variation of the solar wind itself, whereas the comparison between >5.2 keV nose and anti-nose ENAs and nose ions suggested that the modulation of superthermal ions over the solar cycle is global throughout the heliosheath (Dialynas et al. 2017a, 2017b). Schwadron & Bzowski (2018) give an alternate explanation related to episodic cooling and heating of the inner heliosheath plasma during periods of large-scale expansion and compression. However, both explanations show that the Cassini/INCA observations will be strongly dependent on the structure of the heliosheath and changes in the solar wind.



Original content from this work may be used under the terms of the [Creative Commons Attribution 4.0 licence](#). Any further distribution of this work must maintain attribution to the author(s) and the title of the work, journal citation and DOI.

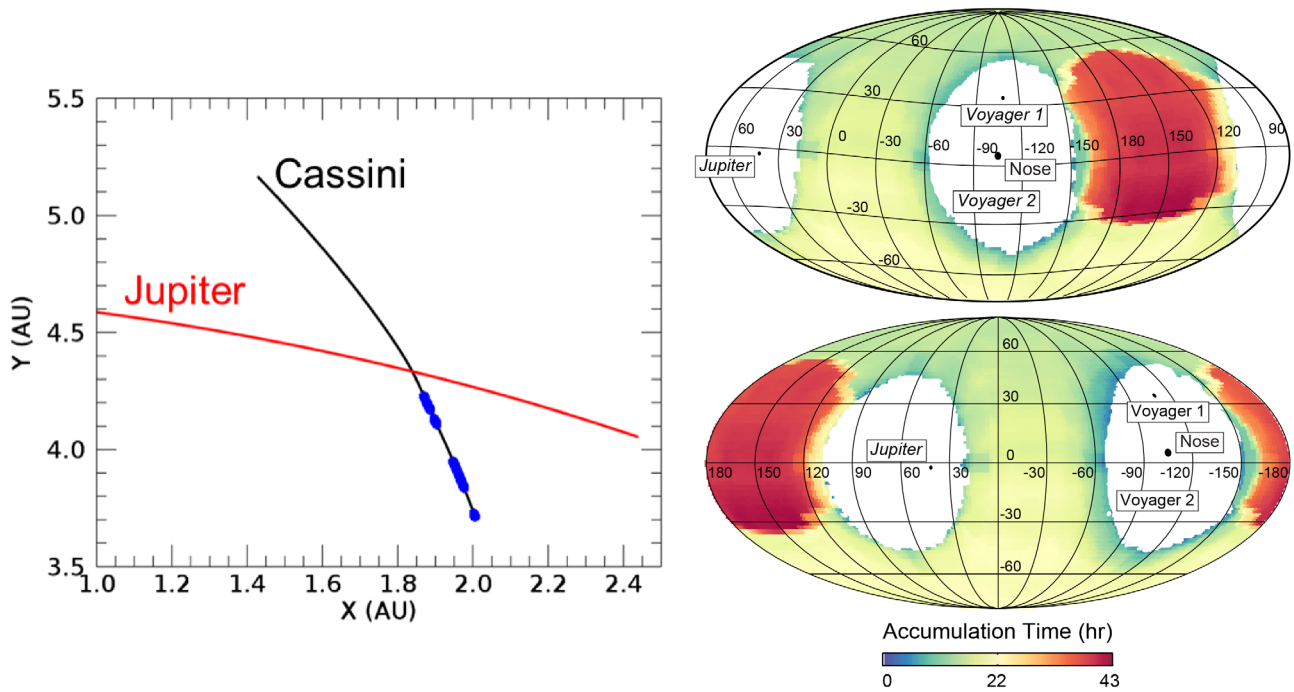


**Figure 1.** Cassini’s trajectory (left) and the total accumulation time maps organized in ecliptic coordinates (right) for the data presented in this study. The full observation consists of a series of time periods that were identified as suitable for imaging the heliosphere during the pre-Jupiter encounter resulting in a maximum total accumulation time of  $\sim 43$  hr toward  $\sim 120^\circ$ – $180^\circ$  in longitude. The left plot shows the trajectory of Cassini and Jupiter from 2000 October 1 to 2000 December 19 in the J2000 coordinate system with blue points indicating the times when the images were taken. The maps to the right show Mollweide projections organized in ecliptic coordinates of the sky centered to the nose (top) and the center of the INCA-defined “Basin” (bottom) with colors indicating the accumulation time in hours. The majority of the map is covered by 22 hr or more of accumulation time resulting in good statistics across most of the sky. There are two large gaps in the map that result from the geometry of the observations with the spinning Cassini high-gain antenna pointed to Earth and also images rejected due to Jupiter’s location in the sky.

As the solar wind varies with the solar cycle, the particles in the outer heliosphere were found to respond on various timescales offset by the substantial travel time from the Sun to the outer heliosphere, and back (Reisenfeld et al. 2016; Dialynas et al. 2017b; McComas et al. 2018). The 2009–2015 IBEX mission maps showed time varying ENA emissions and their relation to the solar cycle (Dayeh et al. 2012; McComas et al. 2018) as did the Cassini/INCA maps (Dialynas et al. 2017b, 2017a). For example, Reisenfeld et al. (2016) investigated ENA variations at the poles, where the contribution of the ribbon, and of relative velocity effects, are weaker, to study how the heliosphere reacts to the solar cycle. This study found that the ENA fluxes at higher energies within the IBEX range are correlated with the areas of the polar coronal holes providing support for the theory that these ENAs originate from pickup ions from the very-high-speed solar wind that emanates from the polar coronal holes.

In this work we present heliospheric ENA observations from the Cassini/INCA ENA instrument during the period prior to Cassini’s flyby of Jupiter in late 2000. This data set spans a time period not covered by any other heliospheric ENA imaging and also provides a unique vantage point in interplanetary space away from background sources.

## 2. Observations

Cassini launched on 1997 October 15 and followed a Venus–Venus–Earth inner solar system tour before flying by Jupiter en route to Saturn (Matson et al. 2003). Prior to the Jupiter flyby, several INCA observations were made of Jupiter and also of large portions of the sky. Due to the focus on the Jupiter observations (e.g., Mauk et al. 2003), the observations of the heliospheric ENAs were largely overlooked. After

further analysis, it is clear that the INCA heliospheric observations prior to the Jupiter flyby represent an important vantage point both in time and in space. Figure 1 shows the trajectory of Cassini during the cruise to Jupiter and out to Saturn along with the periods where Cassini attained heliospheric images.

The Cassini/INCA instrument is a large geometric factor slit geometry ENA imager (Krimigis et al. 2004). INCA observes ions and ENAs over the energy range  $5 \text{ keV nuc}^{-1} < E < 3 \text{ MeV nuc}^{-1}$  with directional knowledge better than  $4^\circ$  FWHM. In this study, we utilize four hydrogen ENA energy bands that span 5.2–13.5 keV, 13.5–24 keV, 24–35 keV, and 35–55 keV. The convention for the Cassini/INCA energy ranges differs from that of IBEX-Hi due to the measurement technique applied. For IBEX-Hi the energies are quoted as the central energy within an energy band defined with edges that are defined by the FWHM of the combined system efficiency. For Cassini/INCA the energy ranges are defined by the particle time-of-flight acceptance within the channel and since the efficiencies are relatively flat across the channels we report the range of energies contained in the channel. In ENA mode, INCA rejects ambient ions using an array of serrated deflector plates with alternating positive and negative potentials applied, effectively sweeping energetic charged particles with energies up to  $\sim 150 \text{ keV e}^{-1}$  into the plate walls.

INCA’s extended field of view (FOV) produces images of large swaths of the sky. The INCA design is suited to three-axis stabilized spacecraft and is capable of imaging an angular region  $90^\circ \times 120^\circ$ . The FOV of the INCA instrument in its time-of-flight mode is divided into a  $16 \times 16$  pixel grid. The two rows of pixels near the edge of the FOV have small geometric factors and are excluded from this analysis restricting the total imaging

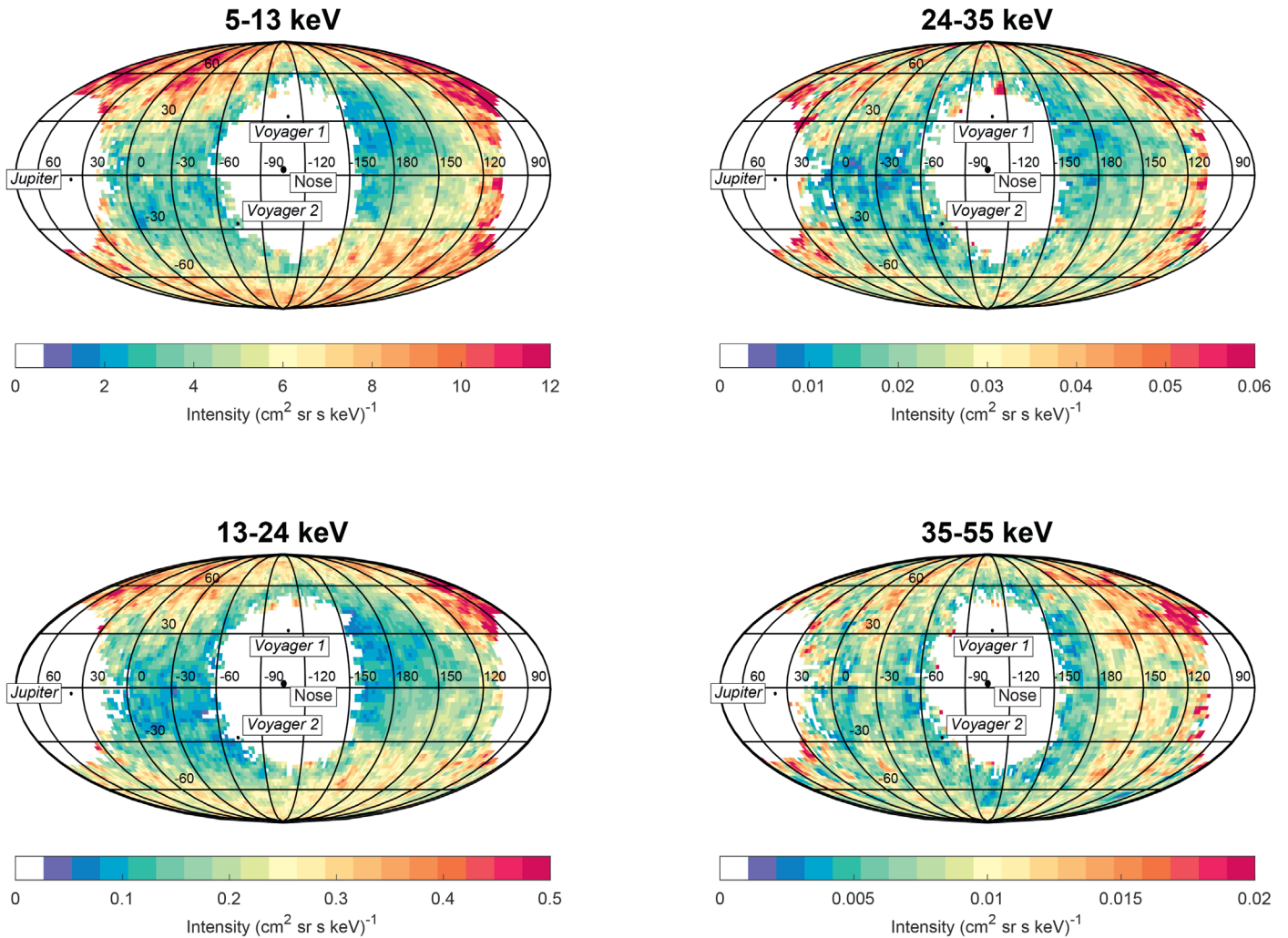


**Figure 2.** Heliospheric ENA intensity maps as measured by Cassini INCA en route to Jupiter from 2000 October 2 to 2000 December 21 over four energy bands. The maps are plotted using a Mollweide projection, organized in ecliptic coordinates, centered on the heliospheric nose with the locations of the Voyager 1 and 2 spacecraft are noted. The locations of the Voyager 1 and 2 spacecraft are also indicated in the figures. The maps are produced from four energy bands in INCA covering energies from 5.2 to 55 keV. The 5.2–13.5 keV energy channel is focused within the interstellar PUI energy range, while the three higher energies (13.5–24 keV, 24–35 keV, and 35–55 keV) reflect suprathermal populations. These plots are rotated to be in a similar orientation to previous IBEX studies. In presenting this data we have adopted similar colorbar limits to previous studies that use the INCA data so that the intensities can be easily compared. We did however change the color structure of the colorbar away from the commonly used rainbow-type colors to a color structure that has sequential colors and is colorblind-friendly (Brewer et al. 2003).

surface to a  $12 \times 12$  grid and maintaining a geometric factor of  $1.0 \text{ cm}^2 \text{ sr}$  (calculated as  $144 \text{ pixels} \times 0.007 \text{ cm}^2$  per pixel). Standard Cassini/INCA calibrations (Krimigis et al. 2009; Dialynas et al. 2017a) have been utilized for these maps. The systematic errors of this data are roughly  $\pm 20\%$  range based on comparisons with the in situ ion instruments on board Cassini (MIMI/CHEMS and MIMI/LEMMS; Dialynas et al. 2013).

From 2000 October 2 to 2000 December 21, the Cassini/INCA instrument produced heliospheric ENA measurements on approach to Jupiter. The sky coverage, shown in Figure 1, is fairly comprehensive with significant gaps in the sunward direction and some gaps in the direction of Jupiter, where the ENA images could be contaminated by ENAs from Jupiter. We also remove images during times where significant quantities of ions are present in the vicinity of Cassini as measured by the MIMI/CHEMS instrument. We removed a few time periods where substantial upstream ions are observed emanating from Jupiter. Images from these time frames are taken together to produce the maps shown in Figures 2 and 3. In addition, to

eliminate pixels with low counting statistics Figures 2 and 3 only plot pixels with over 25 counts in the pixel for the 5–13 keV and 13–24 keV channels and over 10 counts in the pixel for the 24–35 keV and 35–55 keV channels. We also plot the raw counts over the sky in Figure 4 showing the regions of the sky that have good counting statistics.

Each observation contains some data taken while the Cassini spacecraft is rolling about the  $z$ -axis (about the high-gain antenna) and some where it is in a fixed orientation. The INCA instrument produces onboard calculations during a roll observation to accurately place events within a larger image (Krimigis et al. 2009; Dialynas et al. 2013). This way a single observation can take place and the motion of the spacecraft is compensated by the INCA processing.

### 3. Results

The general structure of the ENA maps follows a pattern similar to previous studies with enhanced intensities near both

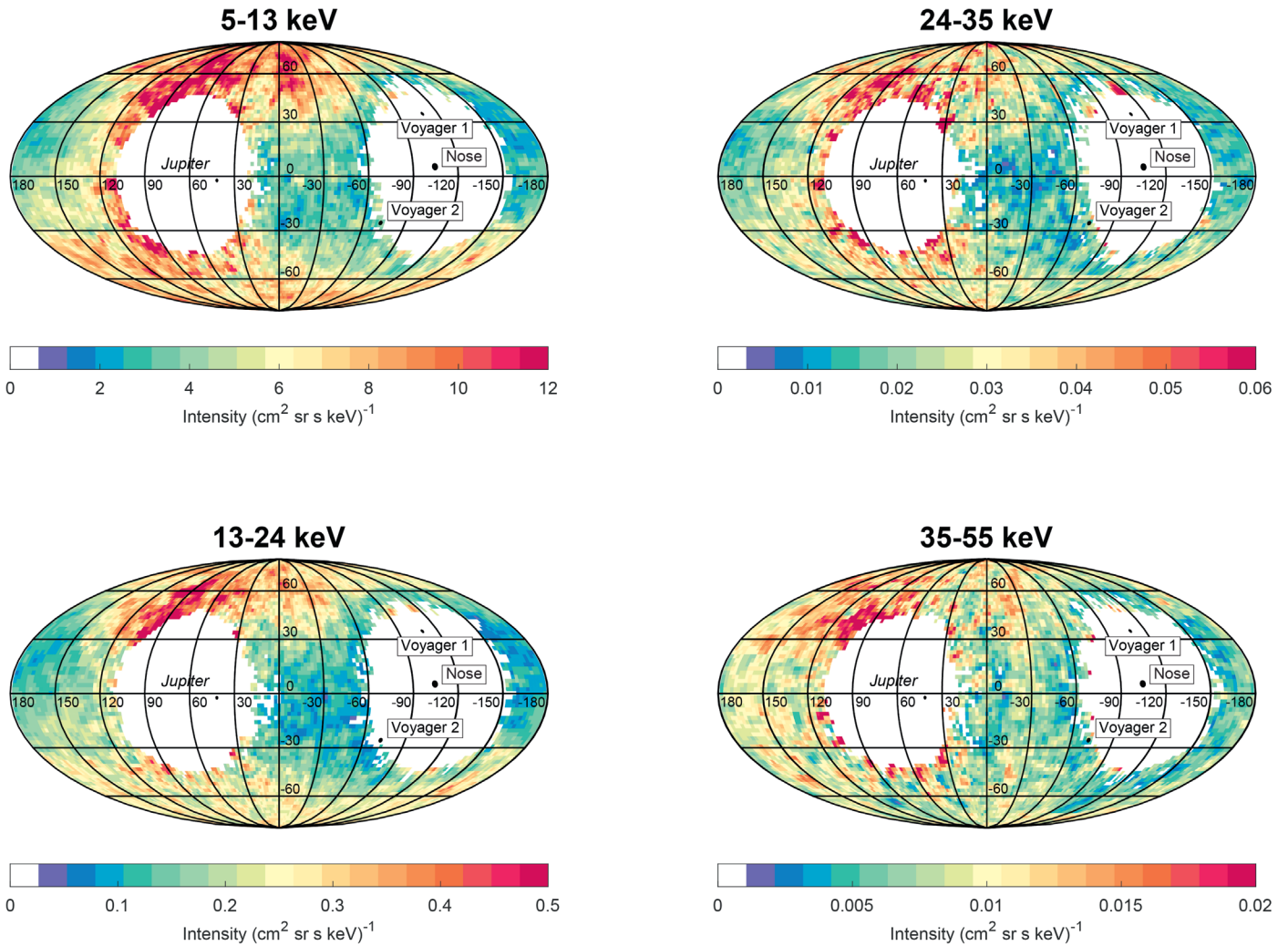


**Figure 3.** Same as Figure 2, except rotated to center on  $0^\circ$  latitude and  $0^\circ$  longitude (rough center of the Cassini/INCA-defined “Basin”). We provide two viewpoints of the data for comparison to the previous Cassini/INCA maps that have been plotted in this way.

poles and toward the anti-nose direction as well as large swaths of low intensities, referred to as the basins or lobes, near the equatorial regions and on the flanks (e.g., Krimigis et al. 2009; Dialynas et al. 2013). The 5.2–13 keV INCA measurement distinctly shows this polar/equatorial dichotomy, i.e., the equatorial basin, with this feature becoming somewhat less pronounced at higher energies. The 35–55 keV map lacks sufficient statistics to truly identify any substantial deviations from about  $0.01 \text{ cm}^{-2} \text{ sr}^{-1} \text{ s}^{-1} \text{ keV}^{-1}$ .

The Cassini/INCA maps produced by Dialynas et al. (2017a) from 2003 to 2014 showed some latitudinal structure with many maps having enhanced emissions near the north pole. However, the most constant feature within these maps was a longitudinal structure at mid-latitudes with enhanced intensities near the nose and anti-nose direction. The peak intensities occurred near  $80^\circ$  and  $-70^\circ$  longitude in the latitude band between  $\pm 39^\circ$ . In comparison to the maps shown in Figures 2 and 3 the coverage of these peaks is unfortunately incomplete. This longitudinal structure is similar to the Cassini/INCA maps published earlier in the literature, especially in the 2013 map (Dialynas et al. 2017a). The year 2013 happens to be in a similar phase of the 11 year solar cycle as the maps presented in Figures 2 and 3 taken in 2000; both maps were taken within the rise of their respective solar cycles.

The general structure of the 5.2–13.5 keV map also appears consistent with the IBEX maps produced in the highest-energy bins near solar maximum (the 2012 and 2013 maps, specifically the “B” maps taken during the second half of the year; McComas et al. 2017) of the IBEX-Hi instrument, where the highest intensities are consistently at the poles with large swaths of low intensity at low latitudes (McComas et al. 2017). Detailed comparisons of the INCA maps with the IBEX maps are detailed in Dialynas et al. (2013). We note that the top energy of IBEX-Hi is close to the lowest-energy INCA channel, though in reality any overlap between the two is limited due to the decreased efficiencies at the lowest energy of the INCA channel and at the highest energy of the IBEX-Hi channel. The IBEX maps presented by McComas et al. (2017) show a similar anti-nose or tailward enhancement in the 2.73 keV (1.99–3.75 keV) and 4.29 keV (3.13–6.0 keV) maps, with intensities (with the caveat noted earlier with regards to the early calibration of Cassini/INCA fluxes early in the mission) similar to those presented here ( $\sim 10$  ENAs per  $\text{cm}^2 \text{ s keV}$ ). This characteristic, i.e., the overall similarity between the IBEX-Hi/4.29 keV and INCA/5.2–13.5 keV intensities and their distribution in the global sky sphere, was previously identified and discussed in Dialynas et al. (2013) and is a key impetus for the upcoming Interstellar Mapping and Acceleration Probe (IMAP) mission (McComas et al. 2018), which will have full

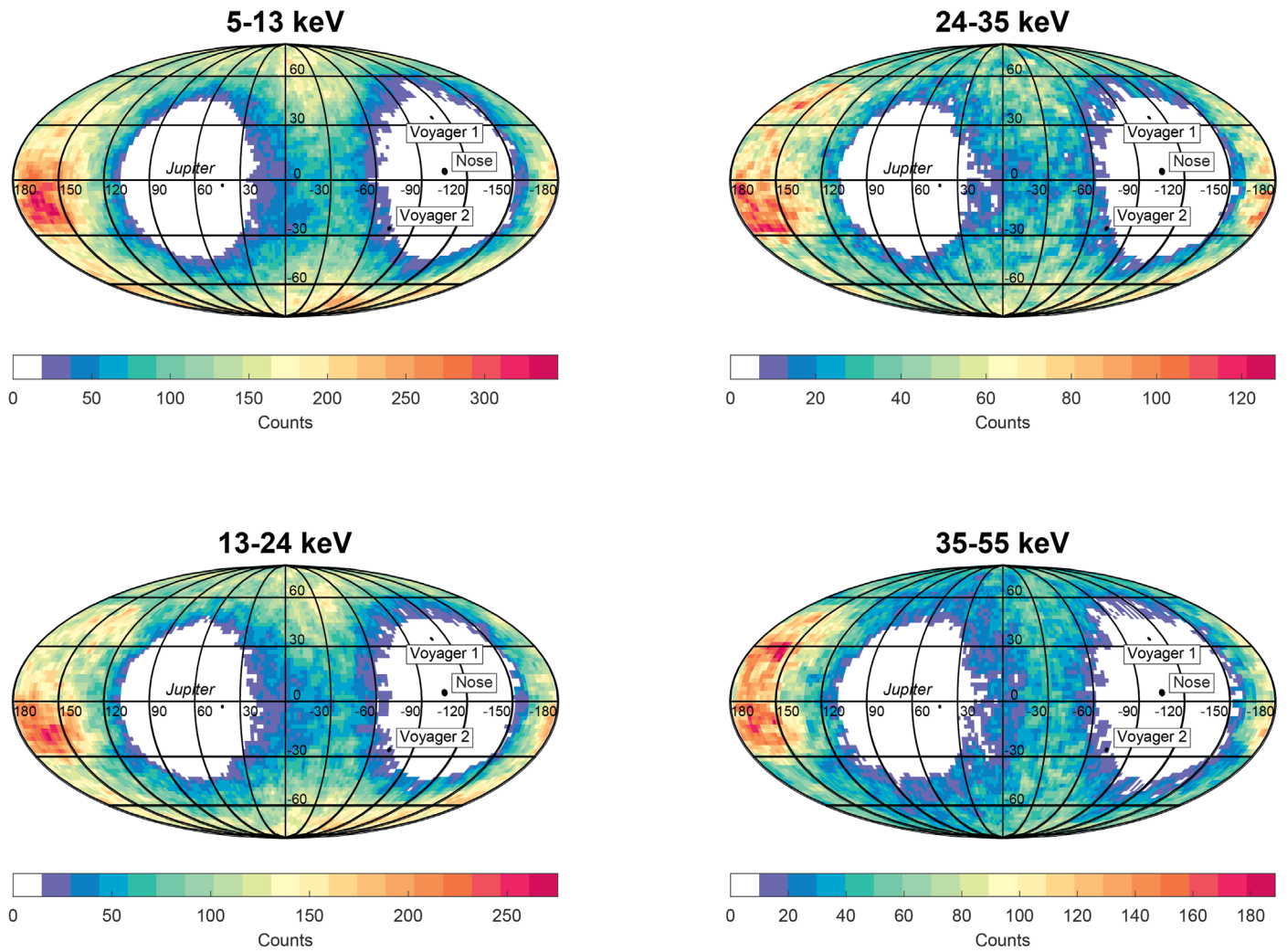


Figure 4. Same as Figure 3, except now plotting the counts in each pixel.

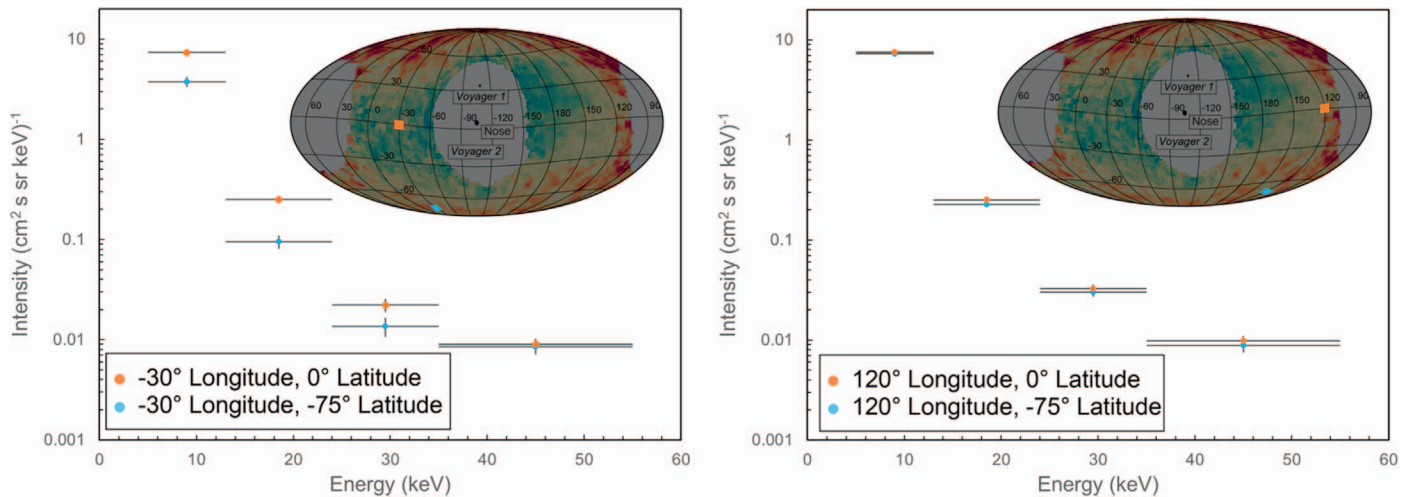
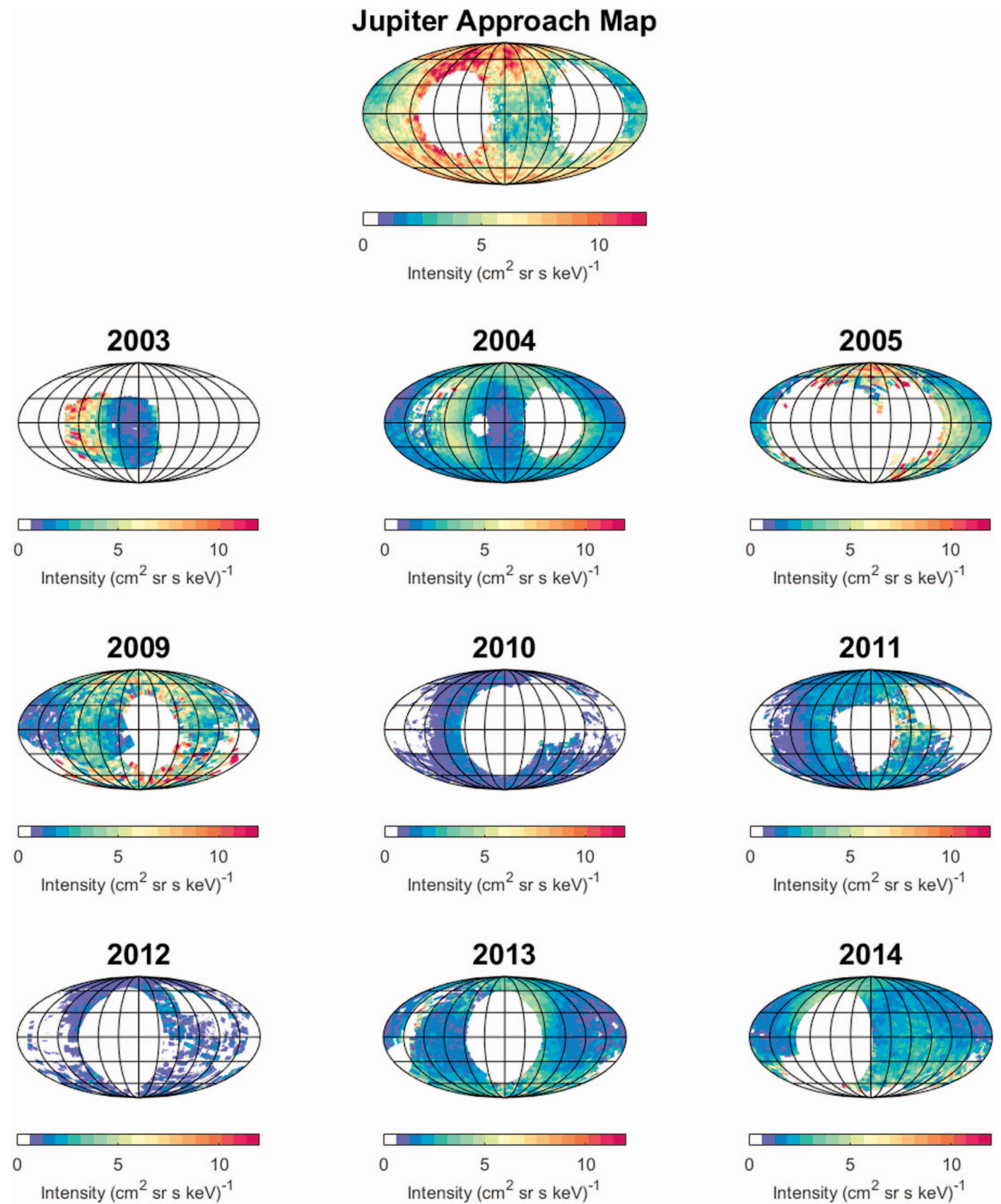


Figure 5. A comparison of the intensity spectrum of the ENAs observed from four locations showing the greater intensities seen at high latitudes. The two panels show a comparison of the high-latitude (blue points) with the low-latitude (orange points) data. Each point represents four adjacent pixels in the map. The sampled locations are shown in the inset maps. The left panel shows a mid- and a high-latitude sampling at  $-30^\circ$  longitude, while the right panel is at  $120^\circ$  longitude. The horizontal bars show the width of the Cassini/INCA energy bins with a point placed in the midpoint of the measured energy in each energy channel. The Poisson statistical error for each point is plotted as the vertical errors and is between 7% and 21% for each pixel.

energy range coverage and a careful cross-calibration between ENA imagers. In addition, previous studies by Dialynas et al. (2013, 2019) and Schwadron et al. (2011) show a spectral break

between the IBEX-Hi and Cassini/INCA measurements with the  $>5.2$  keV ENA energy spectra being softer than the corresponding IBEX-Hi spectra.



**Figure 6.** The new 5–13 keV map taken during the Cassini Jupiter flyby compared to those taken in orbit about Saturn and previously presented by Dialynas et al. (2017) plotted using the same color scale on all plots and the same projection.

Figure 5 shows a comparison of the mid- and high-latitude ENA intensities from two different longitudes. The highest intensities of ENAs generally occur poleward of  $45^\circ$  latitude in both the northern and southern hemispheres for all four Cassini/INCA energy channels. The equatorial latitudes show large regions of low ENA emissions. The lower-energy channels show large differences (factor of 3–5) between the equatorial latitudes and the poles, while in the highest-energy bin the distribution shows no discernible difference between the equatorial and polar regions.

These maps show longitudinal differences (Figure 5) with greater fluxes of ENAs appearing at positive longitudes (toward the anti-nose direction) and lower fluxes appearing at negative longitudes (toward the nose direction) with deep minima on the flanks. This asymmetry is more prevalent in the lower-energy maps. It is unfortunate that this vantage point resulted in the two large blind spots in the direction of the heliospheric nose and anti-nose directions. However, we do have good statistics in the surrounding regions that show enhanced fluxes in the anti-nose or tailward direction and reduced fluxes in the nose direction with deep basins or lobes on the flanks.

We caution interpretation in the few regions within the plots that have relatively low statistics. For example, the spacecraft roll executed during the observations produced a wide band of high accumulation times with the edges having much less accumulation time. These areas of low statistical certainty are at the edges of the two blank areas in the maps and appear as ringed structures in the maps that are dominated by low counts and should not be trusted. In general regions that appear in the blues to purples in Figure 1 only have a few hours of observation time and thus few counts to work with.

#### 4. Discussion and Conclusions

These maps shown in Figures 2 and 3 appear consistent with maps presented by previous Cassini/INCA studies (Dialynas et al. 2017a). The longitudinal and latitudinal asymmetries show distinct enhancements in the anti-nose or tailward and polar regions, which is similar to the structures observed in maps produced in the 2012 time period (Dialynas et al. 2017a) during a similar time in the solar cycle. Both the observations presented here and those from 2012 show a distinct reduced flux in the nose direction. In addition, these maps have similarities to the IBEX maps (McComas et al. 2017) such as the poleward enhancements and distinct basins or lobes on the flanks. These new maps also show a similar tailward or anti-nose enhancement as is seen in the IBEX-Hi maps in the 2.73 and 4.29 keV channels.

These ENA distributions appear to be reflective of particle distributions within the inner heliosheath and generally consistent with the hypothesis that polar emissions coincide with the fast solar wind emitted from solar coronal holes (e.g., Dayeh et al. 2012; Dialynas et al. 2017a). The Voyager 1 and 2 observations showed a prevalence of suprathermal ions beyond the termination shock (Decker et al. 2005). Sokół et al. (2015) produced a long time-base data set with the solar wind speed versus heliolatitude based on interplanetary scintillation data. These observations show the prevalence of high-speed flows at high heliolatitude from the solar minimum around 1997 up to the rise of solar cycle 23, which peaked around 2000–2002. The flow speed at the poles reaches speeds up to about  $800 \text{ km s}^{-1}$  ( $3.3 \text{ keV H}^+$ ). This places the bulk of the solar wind distribution near the poles at the edge of the INCA energy acceptance, and with additional heating at the termination shock places this distribution within the INCA energy range.





Interestingly, these maps show a distinct north/south asymmetry with greater intensities coming from the northern latitudes than from the southern latitudes. This could be linked to the structure of the solar wind with greater intensities or harder spectra in the north than in the south.

In 1999 and 2000, during the Jupiter-approach observations, the solar wind speed was on average much slower at  $\sim 500 \text{ km s}^{-1}$  across all heliolatitudes; however, there is a significant transit time from the Sun to the outer heliosphere and back to Cassini. The response time for ENAs in the inner heliosheath is  $\sim 2\text{--}3 \text{ yr}$  (Dialynas et al. 2017b). This means that ENA observations taken in late 2000 should be observing the effects of the solar wind as it was in late 1997–1998. During this time the Sun was in solar minimum and the onset of SC23 with the regions above  $\sim 20^\circ\text{--}30^\circ$  latitude was dominated by the fast solar wind (e.g., Sokół et al. 2015).

These observations are from late 2000 during the peak of solar cycle 23, when no other instrument was observing the heliospheric structure in ENAs. The majority of the IBEX maps of the heliosphere reported to date occurred during the much weaker solar cycle 24. On the other hand, previous Cassini studies included limited 2003 observations on approach to Saturn in the declining phase of solar cycle 23 and early in the Cassini mission up to 2009 (Krimigis et al. 2009; Dialynas et al. 2013), included more measurements over the onset of SC24 over the 2003–2014 time period (Dialynas et al. 2017a), and finally spanned through the year 2016 (Dialynas et al. 2019) before the Cassini mission end (2017 September 15). Figure 6 shows this new map from late 2000 along with the maps from 2003 to 2014 on the same color scale for the 5–13 keV channel. However, unlike the Jupiter-approach maps shown in Figures 2 and 3, the INCA maps on approach to Saturn had limited coverage due to the substantial obscuration of the sky by Saturn and the Sun convolved with the orbit of Cassini. In addition, the maps presented here are novel because they comprise images obtained from interplanetary space, far away from magnetospheric sources. As such, these INCA observations represent a clean observation of the heliospheric structure in the PUI and suprathermal ion energy ranges.

This research was supported in part by the NASA Office of Space Science under task order 003 of contract NAS5-97271 between NASA Goddard Space Flight Center and the Johns Hopkins University and by subcontract at the Office for Space Research and Technology.

#### ORCID iDs

J. H. Westlake  <https://orcid.org/0000-0003-0472-8640>  
 M. Gkioulidou  <https://orcid.org/0000-0001-9979-2164>  
 K. Dialynas  <https://orcid.org/0000-0002-5231-7929>  
 I. J. Cohen  <https://orcid.org/0000-0002-9163-6009>  
 D. L. Turner  <https://orcid.org/0000-0002-2425-7818>  
 A. K. Higginson  <https://orcid.org/0000-0003-1380-8722>  
 C. P. Paranicas  <https://orcid.org/0000-0002-4391-8255>

#### References

- Brewer, C. A., Hatchard, G. W., & Harrower, M. A. 2003, *Cartography Geogr. Inf. Sci.*, 30, 5  
 Burlaga, L. F., Ness, N. F., Berdichevsky, D. B., et al. 2019, *NatAs*, 3, 1007  
 Burlaga, L. F., Ness, N. F., & Stone, E. C. 2013, *Sci*, 341, 147  
 Dayeh, M. A., McComas, D. J., Allegrini, F., et al. 2012, *ApJ*, 749, 50  
 Decker, R. B., Krimigis, S. M., Roelof, E. C., et al. 2005, *Sci*, 309, 2020  
 Dialynas, K., Krimigis, S. M., Decker, R. B., & Mitchell, D. G. 2019, *GeoRL*, 46, 7911

- Dialynas, K., Krimigis, S. M., Mitchell, D. G., Decker, R. B., & Roelof, E. C. 2017a, *NatAs*, **1**, 0115
- Dialynas, K., Krimigis, S. M., Mitchell, D. G., Decker, R. B., & Roelof, E. C. 2017b, *JPhCS*, **900**, 012005
- Dialynas, K., Krimigis, S. M., Mitchell, D. G., Roelof, E. C., & Decker, R. B. 2013, *ApJ*, **778**, 40
- Funsten, H. O., Allegrini, F., Crew, G. B., et al. 2009, *Sci*, **326**, 964
- Fuselier, S. A., Allegrini, F., Funsten, H. O., et al. 2009, *Sci*, **326**, 962
- Gruntman, M., Roelof, E. C., Mitchell, D. G., et al. 2001, *JGR*, **106**, 15767
- Gurnett, D. A., & Kurth, W. S. 2019, *NatAs*, **3**, 1024
- Gurnett, D. A., Kurth, W. S., Burlaga, L. F., & Ness, N. F. 2013, *Sci*, **341**, 1489
- Heerikhuisen, J., Pogorelov, N. V., Zank, G. P., et al. 2009, *ApJL*, **708**, L126
- Krimigis, S. M., Decker, R. B., Roelof, E. C., et al. 2013, *Sci*, **341**, 144
- Krimigis, S. M., Decker, R. B., Roelof, E. C., et al. 2019, *NatAs*, **3**, 997
- Krimigis, S. M., Mitchell, D. G., Hamilton, D. C., et al. 2004, *SSRv*, **114**, 233
- Krimigis, S. M., Mitchell, D. G., Roelof, E. C., Hsieh, K. C., & McComas, D. J. 2009, *Sci*, **326**, 971
- Matson, D. L., Spilker, L. J., & Lebreton, J.-P. 2003, in *The Cassini-Huygens Mission*, ed. C. T. Russell (Dordrecht: Springer), 1
- Mauk, B. H., Mitchell, D. G., Krimigis, S. M., Roelof, E. C., & Paranicas, C. P. 2003, *Natur*, **421**, 920
- McComas, D. J., Allegrini, F., Bochsler, P., et al. 2009a, *SSRv*, **146**, 11
- McComas, D. J., Allegrini, F., Bochsler, P., et al. 2009b, *Sci*, **326**, 959
- McComas, D. J., Allegrini, F., Bzowski, M., et al. 2014a, *ApJS*, **213**, 20
- McComas, D. J., Dayeh, M. A., Funsten, H. O., et al. 2018, *ApJL*, **856**, L10
- McComas, D. J., Lewis, W. S., & Schwadron, N. A. 2014b, *RvGeo*, **52**, 118
- McComas, D. J., Zirnstein, E. J., Bzowski, M., et al. 2017, *ApJS*, **229**, 41
- Reisenfeld, D. B., Bzowski, M., Funsten, H. O., et al. 2016, *ApJ*, **833**, 277
- Richardson, J. D. 2010, in *Heliophysical Processes*, ed. N. Gopalswamy, S. Hasan, & A. Ambastha (Berlin: Springer), 83
- Richardson, J. D., Belcher, J. W., Garcia-Galindo, P., & Burlaga, L. F. 2019, *NatAs*, **3**, 1019
- Schwadron, N. A., Allegrini, F., Bzowski, M., et al. 2011, *ApJ*, **731**, 56
- Schwadron, N. A., & Bzowski, M. 2018, *ApJ*, **862**, 11
- Schwadron, N. A., Bzowski, M., Crew, G. B., et al. 2009, *Sci*, **326**, 966
- Sokół, J. M., Swaczyna, P., Bzowski, M., & Tokumaru, M. 2015, *SoPh*, **290**, 2589
- Stone, E. C., Cummings, A. C., Heikkila, B. C., & Lal, N. 2019, *NatAs*, **3**, 1013
- Stone, E. C., Cummings, A. C., McDonald, F. B., et al. 2008, *Natur*, **454**, 71
- Stone, E. C., Cummings, A. C., McDonald, F. B., et al. 2013, *Sci*, **341**, 150